POLITECNICO
MILANO 1863

SCUOLA DI INGEGNERIA INDUSTRIALE
E DELL'INFORMAZIONE

Aeroacoustic Optimization of Propellers

Tesi di Laurea Magistrale in Aeronautical Engineering - Ingegneria Aeronautica

Carlos Fernández Pereira, 970556

Advisor:
Prof. Alberto Matteo Attilio Guardone

Co-advisors:
Ing. Luca Abergo

Academic year:
2021-2022

Abstract:
This work presents the progress carried out in the coupled CAA-CFD optimization framework inside the open-source multi-physics solver SU2 for cases with axial symmetry like propellers. In this framework the RANS equations are used to solve the flow around the body and the FW-H formulation propagates the pressure fluctuations to the farfield, then an AD-based discrete adjoint computes the sensitivities. The RANS equations are solved using a rotating reference frame (RRF), replacing the unsteady simulation with a steady simulation and a set of rigid rotations, lowering the computational cost. The successful application of periodic boundary conditions along the half-planes of radial symmetry in the CFD simulation opens the possibility of studying multi-blade propellers by just analyzing a single blade. These techniques are applied to an optimization case in which the shape of a propeller blade is modified to reduce the noise signature at a single observer location while keeping the thrust constant. The proposed framework strongly reduces the average sound pressure level (SPL) for a microphone positioned at a distance of ten times the radius.

Keywords: aeroacoustics, optimization, discrete adjoint, propeller noise

1. Introduction

Urban air mobility (UAM) is expected to become a reality in the coming years. Multi-propeller vehicles powered by electric motors will become an alternative transportation method to commute or travel in between nearby cities [5]. These vehicles will fly over residential areas, thus the noise level they produce must meet the requirements posed by the authorities and be low enough to improve their public acceptance.
Obtaining an accurate prediction of the noise is challenging due to its three-dimensional, unsteady and turbulent nature. This problem was first addressed in 1952 by Lighthill [15] to study the noise produced by turbulent jets. Ffowcs-Williams and Hawkings expanded Lighthill's work in 1969 to account for the noise produced by aerodynamic surfaces in arbitrary motion [13] in what is called the FW-H formulation. Di Francescantonio [8] combined the benefits of the FW-H and the Kirchoff formulations to develop a permeable surface aeroacoustic model, it is nowadays known as the permeable FW-H formulation to distinguish it from the original one.
Once the baseline shape of the propeller blade is obtained, the acoustic noise reduction seems to require modifications that are antagonistic with the requested aerodynamic performances [2]. Local blade modifications based on a trial-and-error approach are inefficient and time-consuming. Due to the large number of parameters involved in aerospace design, gradient-based optimization methods using a discrete adjoint formulation are a suitable choice because the computational cost of evaluating the sensitivities is independent of the number of

design variables [18]. Using automatic differentiation (AD) to compute the sensitivities instead of hand differentiation reduces the implementation effort. Moreover, the assumption of frozen turbulence is not required anymore as the turbulence equations can be differentiated algorithmically.
Inside the aeroacoustic community, it is usual to employ scale-resolving simulations such as large-eddy simulation (LES) or variants of the detached-eddy simulation (DES). These types of simulations require a lot of computational power, so they are not practical for optimization purposes, as several direct and adjoint runs are conducted during each optimization simulation. Over the past few years, a lot of interest has been dedicated to assess whether lower fidelity alternatives such as the URANS equations are feasible for optimization [22]. More recently, Guardone et al [17] validated a steady RANS solver with a rotating reference frame (RRF) to study the noise emitted in cases with axial symmetry.
This work presents the progress carried out on the AD-based discrete adjoint framework inside the open source multi-physics suite SU2 for applications to aeroacoustic problems with axial symmetry, continuing the work done by Guardone et al [17]. Section 2 presents the coupled CFD-CAA optimization framework and the computational cost reduction techniques. Section 3 deals with the grid convergence of the reference case. Section 4 presents the verification of the computational cost reduction techniques and the validation of the aeroacoustic sensitivities using the discrete adjoint. The results of the optimization cases are presented in Section 5 while the conclusions are outlined in Section 6.

2. Coupled CFD-CAA Optimization Framework

2.1. CFD Solver: Unsteady Multi-Physics Solver SU2

The open-source software SU2 has been developed to solve multi-physics problems governed by partial differential equations (PDEs) [11]. It is able to simulate compressible and turbulent flows, which are typical in aeronautical problems solving the RANS equations. The governing equations are spatially discretized using the finite volume method on unstructured meshes. Several convective fluxes schemes, such as the Jameson-Schimdt-Turkel (JST) and the second order Roe scheme are implemented. In order to model turbulence the Spalart-Allmaras(S-A) or the Menter Shear Stress Transport (SST) models are available. Moreover, a dual time-stepping method is used to accurately solve unsteady flows. SU2 was specifically developed to deal with PDE constrained optimization problems, its is compatible with the external library CodiPack for differentiating the code [21].

2.2. CAA Acoustic Solver

The acoustic solver implemented in SU2 is based on the Di Francescantonio formulation [8]. It is an extension of the Formulation 1A developed by Farassat [6], which is a solution of the FWH equation [13] for subsonic cases that can be numerically integrated. Both the permeable surface and the solid surface models are implemented.

2.2.1 FWH Equation: Impermeable and Permeable Surface Models

To obtain the FWH equation, the aerodynamic bodies in arbitrary motion are represented by a discontinuity surface defined by the function $f_b = 0$, such that the flow inside the surface is at rest and has the same properties as the undisturbed medium ($p' = 0, \rho' = 0, \boldsymbol{u'} = 0$). This creates a discontinuity on the flow which must be addressed as the derivatives of the flow parameters are needed for the noise computation. The theory of generalized derivatives is used to reach an inhomogeneous wave equation following Lighthill's derivation, but it also includes monopole and dipole source terms which represent the thickness and loading noise contribution as shown in equation (1). A schematic of the solid FWH model is sketched on Figure 1a.

$$\Box^2[c^2(\rho - \rho_0)] = \frac{\partial}{\partial t}[\rho_0 u_n \delta(f_b)] - \frac{\partial}{\partial x_i}[P'_{ij} n_j \delta(f_b)] + \frac{\partial^2 T_{ij} H(f_b)}{\partial x_i x_j} \tag{1}$$

where P'_{ij} is the perturbation stress tensor defined in equation 2.

$$P'_{ij} = P_{ij} - p_0 \delta_{ij} \tag{2}$$

The main drawback of the FWH equation is the computational cost required to assess the effect of the quadrupole source term. Moreover, the discontinuity surface must coincide with the wet surface of the aerodynamic body, which may not be easy to discretize.
Di Francescantonio [8] proposed a formulation which joined the benefits of the Kirchoff [12] and the FWH formulations. The discontinuity surface is chosen arbitrarily outside of the aerodynamic body, it is a permeable

surface instead of a solid one. Therefore, the non penetration condition does not hold along this fictitious surface, so the local fluid velocity normal to the surface is not null ($u_n \neq 0$) and the local normal velocity of the source surface is not null either ($v_n \neq 0$), so it cannot be assumed that ($u_n - v_n$) is null anymore, it is shown in equation (3). A schematic of the permeable FWH model is sketched on Figure 1b.

$$\Box^2[c^2(\rho - \rho_0)] = \frac{\partial}{\partial t}[\rho_0 U_n \delta(f)] - \frac{\partial}{\partial x_i}[L'_{ij} n_j \delta(f)] + \frac{\partial^2 T_{ij} H(f)}{\partial x_i x_j} \tag{3}$$

The parameters U_i and L_{ij} are defined in equation (4) and can be interpreted as a modified velocity and stress tensor respectively. If the discontinuity surface is chosen to be surface of the aerodynamic, the equation (3) turns into the classical FWH equation shown in (1).

$$U_i = u_i + [(\rho/\rho_0) - 1](u_i - v_i) \tag{4a}$$

$$L_{ij} = P'_{ij} + \rho u_i (u_j - v_j) \tag{4b}$$

The Di Francescantonio formulation has the advantage that if the turbulent structures are properly resolved inside the permeable discontinuity surface, the effect of the quadrupole term can be neglected, so it does not need to be computed.

To obtain an integral formulation of the problem is presented in equation (5), a Green function was used following the approach of Farassat [6] to obtain a permeable version of the Formulation 1A. This formulation assumes that the contribution quadrupole terms outside the discontinuity surface is negligible, hence the pressure fluctuations at an observer location are the sum of the thickness and loading noise. If the impermeable surface model is used, this hypothesis is only reasonable for low Mach problems, in cases with transonic phenomena such as shocks this assumption is not valid anymore. It is also assumed that the disturbances at the observer location are small. Therefore, the quantity affected by the wave operator can be substituted by the pressure fluctuation at the observer location ($c^2(\rho - \rho_0) = p'$).

$$\begin{aligned} 4\pi p' = &\int_S \left[\frac{\rho_0(\dot{U}_i n_i + U_i \dot{n}_i)}{r|1 - M_r|^2}\right]_{ret} dS + \int_S \left[\frac{\rho_0 U_i n_i K}{r^2|1 - M_r|^3}\right]_{ret} dS \\ &+ \frac{1}{c}\int_S \left[\frac{\dot{F}_i \hat{r}_i}{r|1 - M_r|^2}\right]_{ret} dS + \int_S \left[\frac{F_i \hat{r}_i - F_i M_i}{r^2|1 - M_r|^2}\right]_{ret} + \frac{1}{c}\int_S \left[\frac{\dot{F}_i \hat{r}_i K}{r^2|1 - M_r|^3}\right]_{ret} dS \end{aligned} \tag{5}$$

$$K = \dot{M}_i \hat{r}_i r + M_r c - M^2 c \tag{6a}$$

$$F_i = L_{ij} n_j \tag{6b}$$

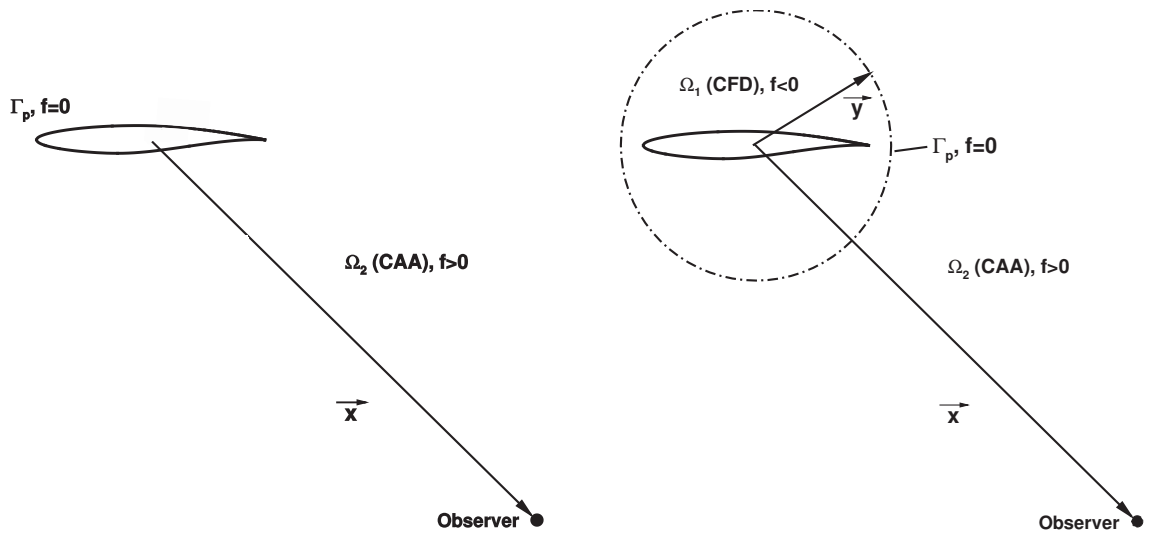

(a) Impermeable Surface Model

(b) Permeable Surface Model

Figure 1: FWH Formulation Schematic [22]

2.3. Computational Cost Reduction Techniques

2.3.1 Rotating Reference Frame (RRF)

In cases which have axial symmetry, like a rotor in hover or a propeller in forward flight, a rotating reference frame moving with the body can be used to reduce the computational cost of both the CFD and the acoustic simulation [9]. First, a steady flow simulation which accounts for the movement of the body with respect to the freestream is conducted. Then, a rotation is applied to the steady solution to obtain the state variables at each time step [17]. This results in a significant reduction of the computational cost because the unsteady simulation is replaced by a steady simulation and a set of rigid rotations.

$$\begin{bmatrix} d\theta \\ d\phi \\ d\psi \end{bmatrix} = \boldsymbol{\Omega} \cdot dt \tag{7}$$

Ω is the constant angular velocity and $d\theta, d\phi, d\psi$ are the incremental angles for each axis. The rotated surface coordinates, grid velocity and normals at each time step are indicated by the hat superscript ($\hat{}$). $\boldsymbol{R}$ is the rotation matrix described in (9).

$$\hat{\boldsymbol{x}} = \boldsymbol{R} \cdot \boldsymbol{x} \tag{8a}$$

$$\hat{\boldsymbol{u}}_{\boldsymbol{grid}} = \boldsymbol{R} \cdot \boldsymbol{u}_{\boldsymbol{grid}} \tag{8b}$$

$$\hat{\boldsymbol{n}} = \boldsymbol{R} \cdot \boldsymbol{n} \tag{8c}$$

$$\boldsymbol{R} = \begin{bmatrix} c\phi c\psi & s\theta s\phi c\psi - c\theta s\psi & c\theta s\phi c\psi + s\theta s\psi \\ c\phi c\psi & s\theta s\phi c\psi + c\theta s\psi & c\theta s\phi c\psi - s\theta s\psi \\ -s\phi & s\theta c\phi & c\theta c\phi \end{bmatrix} \tag{9}$$

2.3.2 Multi-blade Aeroacoustic Analysis using Periodic Boundary Conditions

Conducting the CFD simulation of a multi-blade propeller usually results in a grid with several million elements. This grid may not be feasible for optimization due to the computational cost required for the direct simulation at each step. Since propellers have axial symmetry, the domain can be divided in sectors limited by the planes of radial symmetry. If periodic boundary conditions are applied along them, it is possible to analyze one blade and to account for the effect that the other blades have on the flow. Analyzing this new grid requires a fraction of the cost of the original one. Figure 2 shows an example in which periodic boundary conditions are applied to a two-bladed propeller. In SU2 the solution of the cells located at the *Periodic BC* #1 boundary are copied and rotated 180° to placed them at the *Periodic BC* #2 boundary in each iteration of the flow simulation.

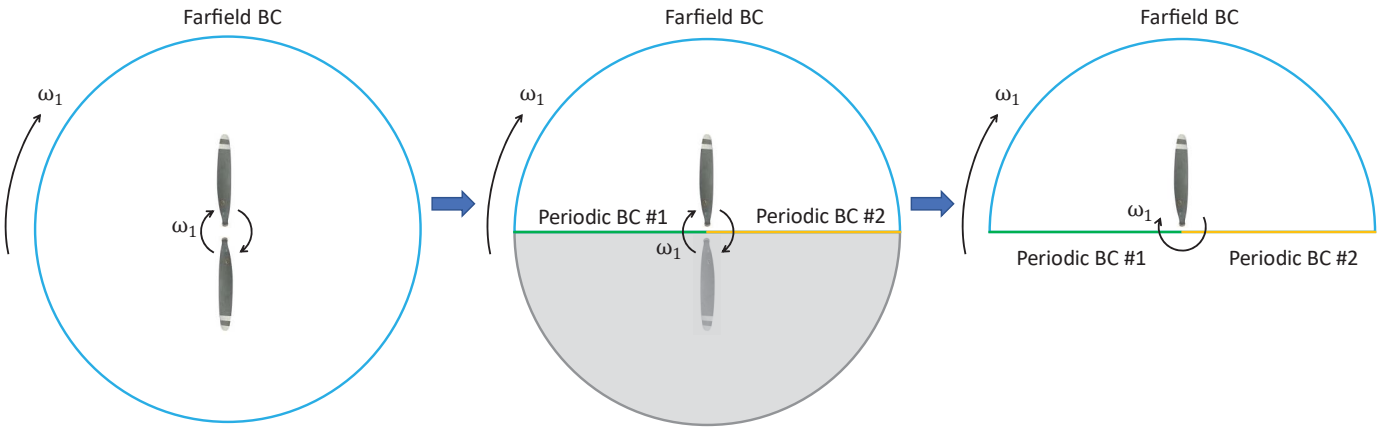

Figure 2: Application of Periodic BC's to a two-bladed propeller

Nevertheless, this approach presents an issue when considering the aeroacoustic analysis. The input for the acoustic solver is the flow at either the immersed body surface (impermeable surface model) or the imaginary surface (permeable surface model). If periodic boundary conditions are used for the CFD simulation, only a fraction of the input data is available. However, the original surface can be reconstructed by placing a copy of the periodic solution in the correct position. Figure 3 shows an example applied to a two-bladed propeller which was analyzed using periodic boundary conditions. Since the impermeable surface model is used, a copy of the surface flow solution is rotated 180° with respect to the origin to recreate the missing blade.

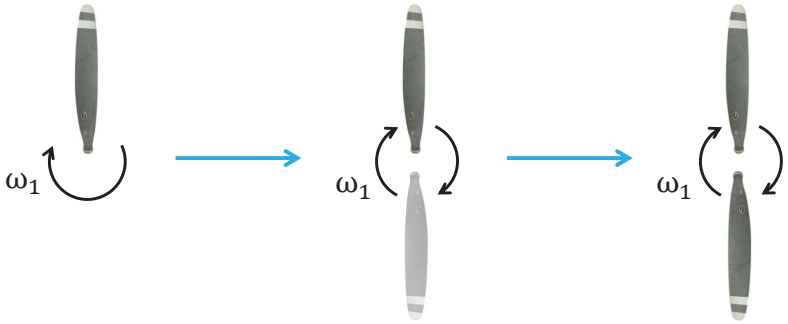

Figure 3: Propeller Reconstruction

2.4. Sensitivity Analysis

The sensitivity analysis consists on computing the derivatives of one or more quantities (outputs) with respect to one or several independent variables (inputs). These derivatives are used in gradient-based optimization to improve the system's performance.
In the case of automatic shape optimization using CFD, the target is to improve a performance parameter called the objective function J by modifying the shape of the immersed body. The shape of the body is parametrized using design variables, a set of parameters stored in a vector α which are under control of the optimizer. They are used to represent the wet surface of the immersed body and its value is changed to modify it and improve the objective function. The aerodynamic domain is discretized by using a grid $X = X_{surf} + X_{vol}$ where $X_{vol} = X_{vol}(X_{surf}(\alpha))$ [16], meaning that the volume grid depends on the surface mesh, which depends itself on the shape of the body. The state variables of the flow field $U(\alpha)$ are analyzed by the solver to assess the convergence criterion using a steady state constraint in pseudo-time. Therefore, it can be noted that both the grid and the flow field state variables depend on the shape of the immersed body.
Consequently, the optimization problem can be written as:

$$\underset{\alpha}{\text{minimize}} \quad J(U(\alpha), X(\alpha)), \tag{10a}$$

$$\text{subject to} \quad R(U(\alpha), X(\alpha)) = 0, \tag{10b}$$

2.4.1 Discrete Adjoint Formulation

The process to reach the expression for the sensitivities follows the approach outlined by Albring et al [4]. As a first step, equation 10b is transformed into a fixed point iteration in pseudo-time such that $U^{n+1} =: G(U^n)$. To handle the surface and mesh deformation, the following constraint is added $X = M(\alpha)$, where M is assumed to be differentiable but no assumptions about its structure are made. Therefore, the optimization problem takes the form:

$$\underset{\alpha}{\text{minimize}} \quad J(U(\alpha), X(\alpha)), \tag{11a}$$

$$\text{subject to} \quad U(\alpha) = G(U(\alpha), X(\alpha)), \tag{11b}$$

$$X(\alpha) = M(\alpha), \tag{11c}$$

To introduce the adjoint formulation, the Lagrangian associated to the optimization problem is used to condense the objective function and the constraints in a single expression. $\bar{U}$ contains the adjoint variables associated to the flow field and $\bar{X}$ contains the adjoint variables associated to the grid geometry.

$$L(\alpha, U, X, \bar{U}, \bar{X}) = J(U, X) + [G(U(\alpha), X(\alpha)) - U(\alpha)]^T \bar{U} + [M(\alpha) - X(\alpha)]^T \bar{X} \tag{12}$$

Differentiating equation (12) with respect to α it is possible to obtain the sensitivities. The value of the Lagrange multipliers is tailored to avoid computing the jacobians $\frac{\partial U}{\partial \alpha}$ and $\frac{\partial X}{\partial \alpha}$. This leads to the following expressions for the computation of $\bar{U}$ and $\bar{X}$.

$$\bar{U} = \frac{\partial}{\partial U} J^T(U, X) + \frac{\partial}{\partial U} G^T(U, X)\bar{U} \tag{13}$$

$$\bar{X} = \frac{\partial}{\partial X} J^T(U, X) + \frac{\partial}{\partial X} G^T(U, X)\bar{U} \tag{14}$$

The equation (13) can be solved by using a fixed-point iteration. By applying the previous steps, the sensitivities of the objective function J take the form.

$$\frac{dL^T}{d\alpha} = \frac{dJ^T}{d\alpha} = \frac{d}{d\alpha} M^T(\alpha)\bar{X} \tag{15}$$

The jacobians present in equations (13) and (14) along with the one present in equation 15 are computed through automatic differentiation (AD) using the reverse mode. Automatic differentiation (AD) applies recursively the chain-rule through the software code to obtain the derivatives. By construction, AD-based adjoints are accurate to machine precision because they do not incur in neither round-off nor truncation error.
Figure 4 shows the chart of the sensitivity computation for the CFD-CAA optimization framework presented in this section. Starting from a specific design variable vector $\alpha^{k=0}$ which corresponds to the baseline propeller shape, during the direct phase, the converged steady state flow U^* is obtained using a rotating reference frame by the CFD solver. Then, the state variables at the solid surface nodes Γ_s are rotated as explained in section 2.3.1 to obtain the flow solution at each time step $U^*(t)$. The, the conservative variables are passed to the FW-H solver to compute the pressure fluctuation $p'(t)$ at a fixed observer position via equation (5) which is used to compute the objective function J.

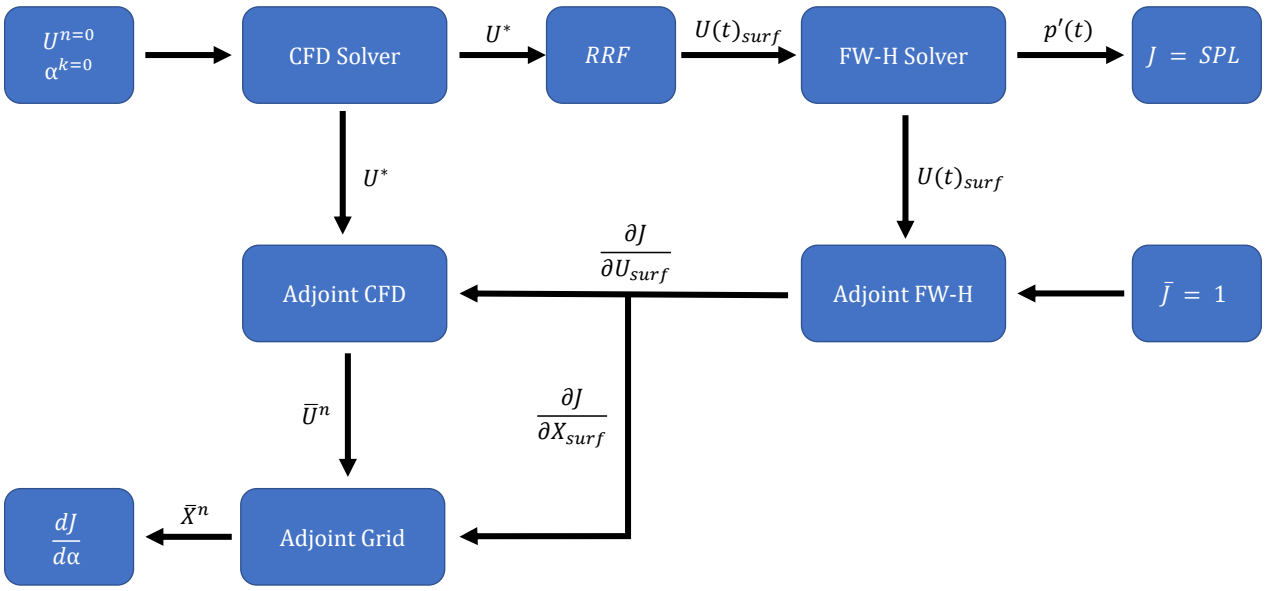

Figure 4: CFD-CAA Sensitivity Computation Chart

During the adjoint phase, the FW-H adjoint solver computes the jacobians associated to the objective function $(\frac{\partial J}{\partial U}, \frac{\partial J}{\partial X})$ and the adjoint CFD solves equation (13) to obtain the flow adjoint variables $(\bar{U})$, the adjoint grid solves equation (14) to obtain the grid adjoint variables $(\bar{X})$. In the end, the geometrical parametrization $M(\alpha)$ is also differentiated to obtain the sensitivies $(\frac{dJ}{d\alpha})$ as in equation (15). The optimizer uses the information given by the sensitivities to update the design variable vector to $\alpha^{k=1}$. Then, the volume grid is updated and a new iteration is started.

3. Baseline Propeller Configuration

The reference case used in this work is a two-bladed propeller. Each blade has a NACA4412 section and a radius $R = 0.114m$. The propeller is investigated in a forward flight condition in which it rotates around the x-axis at $\omega = -523.598$ rad/s. In standard conditions for pressure and temperature the propeller has a tip Mach number of $M = 0.15740$, the free-stream has a velocity of $U = 5m/s$.

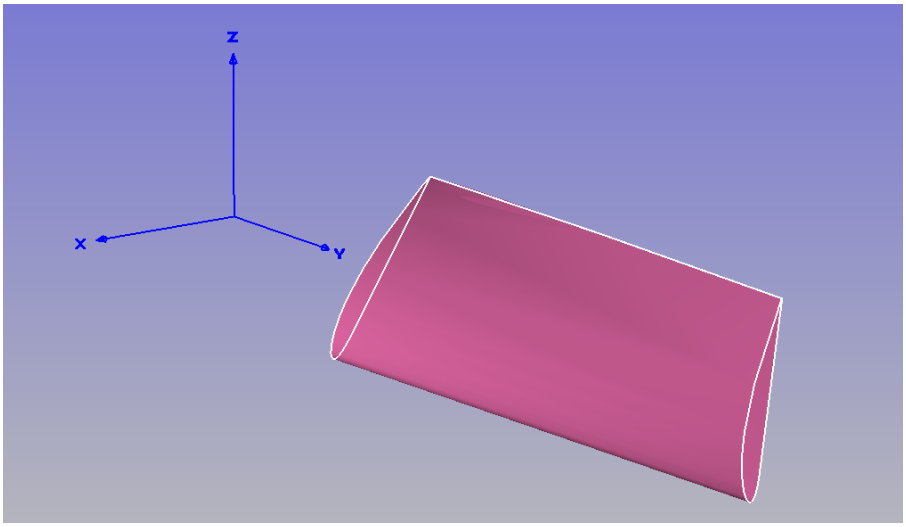

Figure 5: Baseline Propeller Blade

Since the problem has axial symmetry the computational cost reduction techniques explained in section 2.3 are implemented. The unsteady RANS simulation is replaced by a steady RANS simulation and a rotating reference frame (RRF) in solidarity with the blades to reduce the computational cost [10]. Moreover, periodic boundary conditions are implemented on the radial symmetry plane to analyze only one blade and further decrease the computational cost.
The numerical method used to solve the convective fluxes is ROE 1^{st} order, implicit Euler is used to advance the simulation in pseudo-time with a CFL=1. The RANS equations are solved in their dimensional form. The turbulence model used is Spalart-Allmaras (SA), it is solved with a scalar upwind method of first order.

3.1. Grid Convergence

A grid convergence process is conducted to verify that the results are independent from the spatial discretization and to choose a mesh for the subsequent analyses that balances accuracy and computational cost. To carry out the grid convergence analysis, the Index Method [20], [7] has been used. This method provides guidelines both to create the meshes involved in the analysis and to interpret the results. Starting from a baseline mesh, both a finer and a coarser mesh are needed which must satisfy a constraint over the refinement factor r_{ij} given on equation 16 in which h_i is the average cell size of i-th mesh.

$$r_{ij} = \frac{h_i}{h_j} > \sqrt{2} \tag{16}$$

It is not straight forward to compute the average cell size of each mesh, so the following estimation is used $h_i = \sqrt[3]{Vol/N_i}$ to obtain equation 17.

$$r_{ij} = \frac{h_i}{h_j} \approx \sqrt[3]{\frac{N_j}{N_i}} \tag{17}$$

Three different grids are used in the grid convergence process, they share some common features, the grid is cylindrical with a radius $R = 12$m and a length $L = 48$m. They are all hybrid grids, so most of the mesh is unstructured except for a structured part around the blade obtained by extruding the surface mesh along the external normal direction in order to capture the boundary layer correctly. The general characteristics of the structure region along with the number of elements of each grid is summarized in Table 1.

Table 1: Grid Characteristics

	Coarse	Medium	Fine
$\mathbf{N_{elements}}$	1.21 M	1.95 M	4.68 M
Growth Rate	1.25	1.2	1.15
$\mathbf{N_{Layers}}$	25	30	40

Figure 6 shows the convergence of the thrust and moment coefficients, C_{F_x} and C_{M_x} respectively, along with the Richardson extrapolation as $h_{mean} \to 0$. It can be observed that both coefficients converge as the average element size decreases.

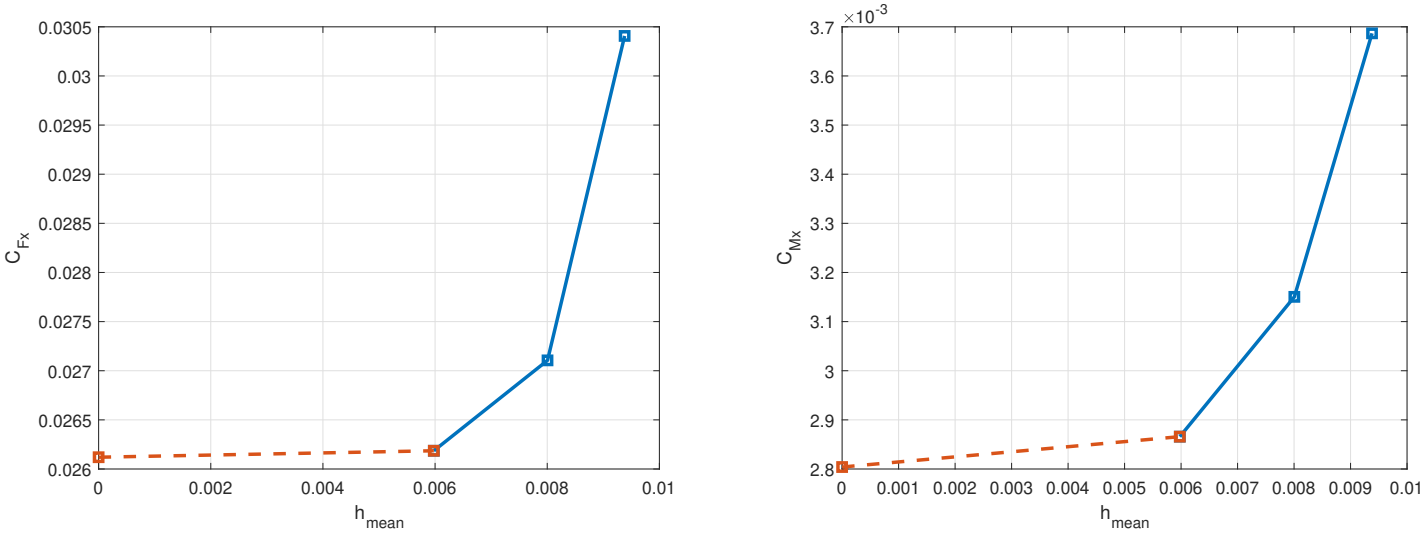

(a) C_{F_x} Convergence

(b) C_{M_x} Convergence

Figure 6: Grid Convergence Criteria

4. Verification & Validation

According to the AIAA guidelines [1], verification is defined as the process of determining that a model implementation accurately represents the developer's conceptual description of the model and the solution to the model. In general, verification aims at identifying, quantifying and reducing the errors of the computational model. This done by using either analytical or very accurate numerical solutions as the basis for the comparison process [19]. Verification is very useful in the early development of a software and as a review procedure for modifications in later stages.
Validation is the process of determining the degree to which a model is an accurate representation of the real world from the perspective of the intended uses of the model [19]. Therefore, the validation process measures numerical accuracy with respect to experimental data, generally with an increasing degree of complexity with each experiment.

4.1. Verification of the Periodic BC's for Aeroacoustic Analysis of Propellers

In order to verify the use of periodic boundary conditions for multi-blade aeroacoustic analysis, the results obtained with the periodic one-blade simulation are compared to the solution obtained using the original two-blade baseline propeller. The periodic case uses a fixed CFL=1 whereas the baseline case uses an adaptive CFL.

Table 2 shows the thrust and moment coefficients (C_{F_x}, C_{M_x}) for each case along with the relative error of the periodic case. It can be noted that the error is smaller than 3% in both cases, so there is a good agreement between both simulations. The source of this error will have to be studied.

Table 2: Coefficients Verification

Parameter	Baseline	Periodic	Rel. Error %
$\boldsymbol{C_{F_x}}$	2.7914×10^{-2}	2.7105×10^{-2}	2.898
$\boldsymbol{C_{M_x}}$	3.2211×10^{-3}	3.1503×10^{-3}	2.198

Figure 7 shows the pressure coefficient (C_P) at the 90% span of the blade for the periodic and baseline cases. It can be observed that there is almost a perfect overlap among the points. By zooming into the points with the smallest C_P it can be noted that there is a slight difference between the two distributions, which gives rise to the small difference in the C_{F_x}, C_{M_x} coefficients. Therefore, it can be concluded that the simulation with periodic conditions solves the flow-field successfully.

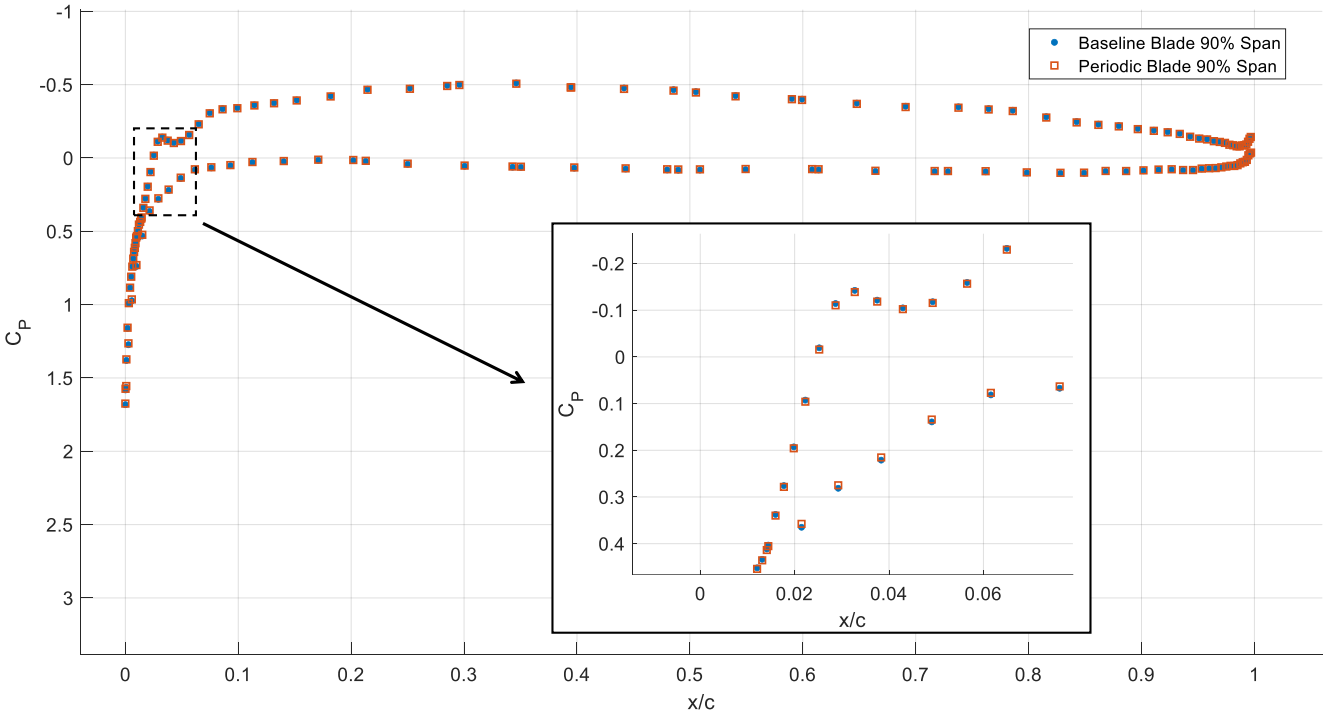

Figure 7: 90% Span C_P Comparison: Baseline Blade vs Blade with Periodic BC's

Regarding the acoustic simulation, the impermeable Di Francescantonio formulation is used, so the acoustic discontinuity surface coincides with the propeller blade surface. The propeller reconstruction technique explained in section 2.3 must be analyzed to verify that it gives the correct results. For that purpose, an array of 10 microphones is placed at a distance $d = 10R$, with R being the radius of the propeller at an incidence angle from 45° to 135° as it is shown in Figure 8.

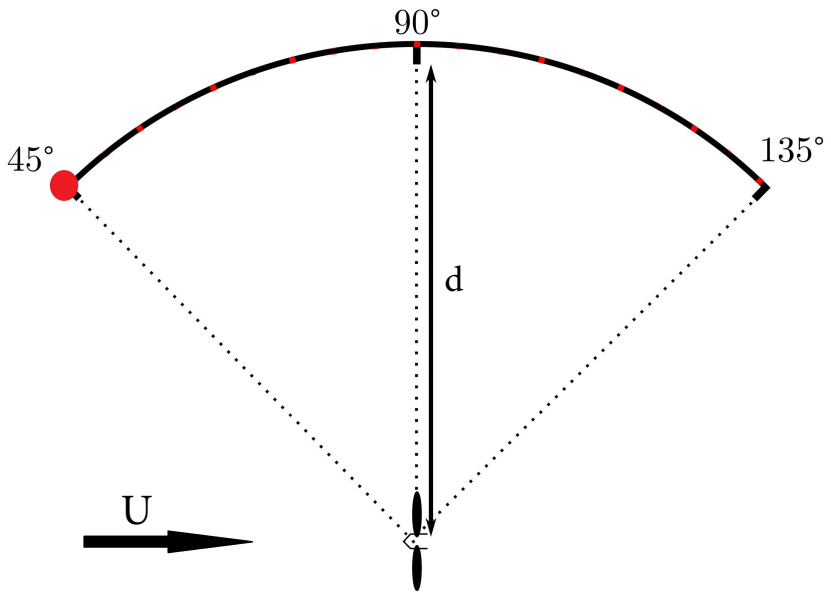

Figure 8: Mic array position with respect to the propeller

The pressure fluctuation and the FFT of the baseline and the periodic cases are analyzed for the observer location at 45° and shown in Figure 9. It can be observed that the signal received in very similar for both cases, being slightly more attenuated in the periodic case. This can be clearly seen in the FFT because the low frequency points in the periodic case have a smaller magnitude.

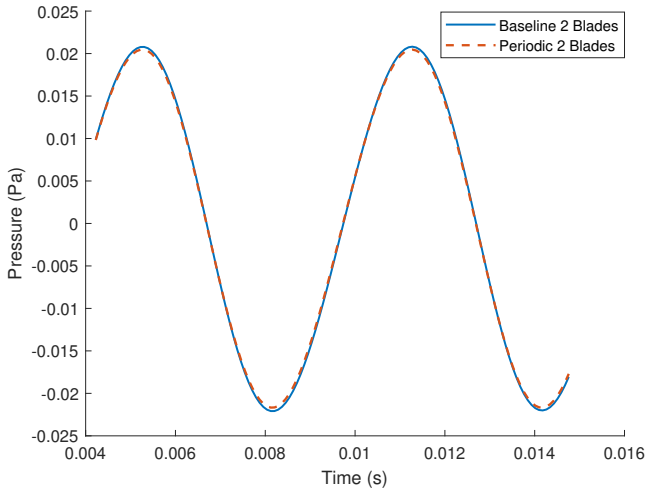

(a) Pressure Fluctuation

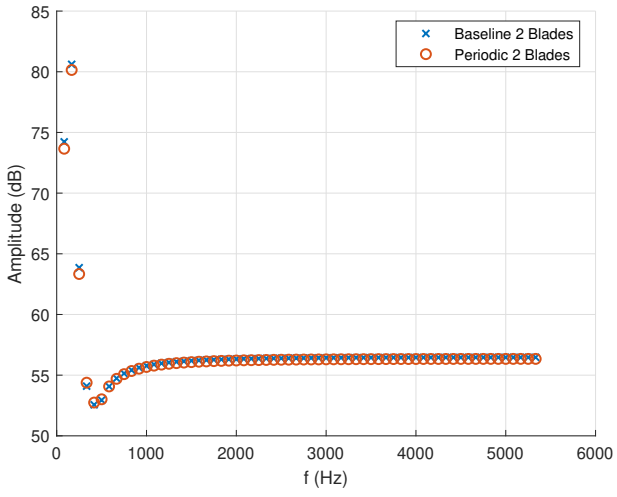

(b) FFT

Figure 9: Acoustic Signature at 45° Observer

The sound pressure level (SPL) and the relative error of the root mean square pressure (p_{rms}) are compared at each observer location. In equation (18), $p'_{n,m}$ is the pressure fluctuation at the observer location, N is the total number of samples and N_* is the number of samples which are not used for the computation of the p_{rms} to avoid errors in the F1A formulation presented in section 2.2 as it uses a retarded-time algorithm [22].

$$p_{rms} = \sqrt{\frac{1}{N - N_*} \sum_{n=N_*+1}^{N} (p'_{n,m})^2} \tag{18}$$

$$SPL = 20\, log_{10}\left(\frac{p_{rms}}{p_0}\right), \quad p_0 = 20\,\mu Pa \tag{19}$$

Figure 10a shows the SPL for both the baseline case and the one with periodic boundary conditions. Figure 10b shows the relative error of the p_{rms} at each observer location. It can be observed that the error of the p_{rms} is around 2% at every observer which is of the same order as the relative errors for the thrust and torque coefficients (C_{F_x}, C_{M_x}) shown in Table 2. Therefore, it can be concluded that the propeller reconstruction technique presented in Section 2.3 works as intended.

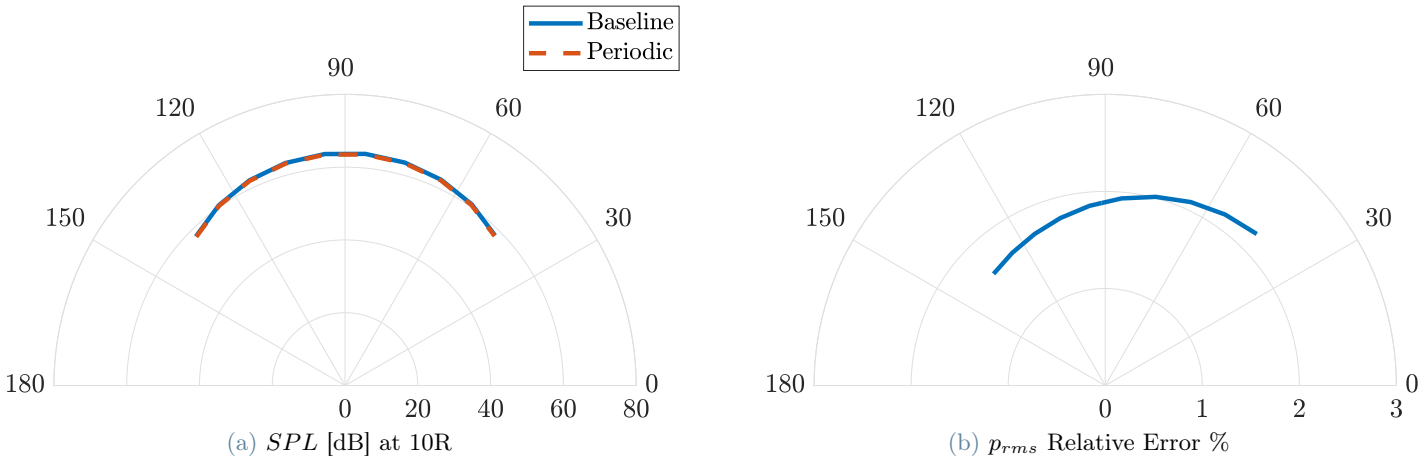

(a) SPL [dB] at 10R (b) p_{rms} Relative Error %

Figure 10: Propeller Acoustic Signature $45° - 135°$ Observers

4.2. Validation of the Adjoint Sensitivities

The sensitivities in the coupled CFD-CAA framework are computed using the discrete adjoint formulation explained in section 2.4.1. They are validated by comparing them to the sensitivities obtained using finite differences. The test-case used for the validation is the baseline case presented in section 2.3. The geometry is parametrized using one FFD box with 24 design variables that can move only along the freestream flow direction (x-axis). Figure 11 shows the comparison of the noise sensitivity for each design variable using the discrete adjoint formulation and finite differences employing the forward mode with two different steps of $h = 10^{-6}$ and $h = 10^{-7}$. It can be observed that there is a very good agreement among the three methods, so the discrete adjoint formulation is validated.

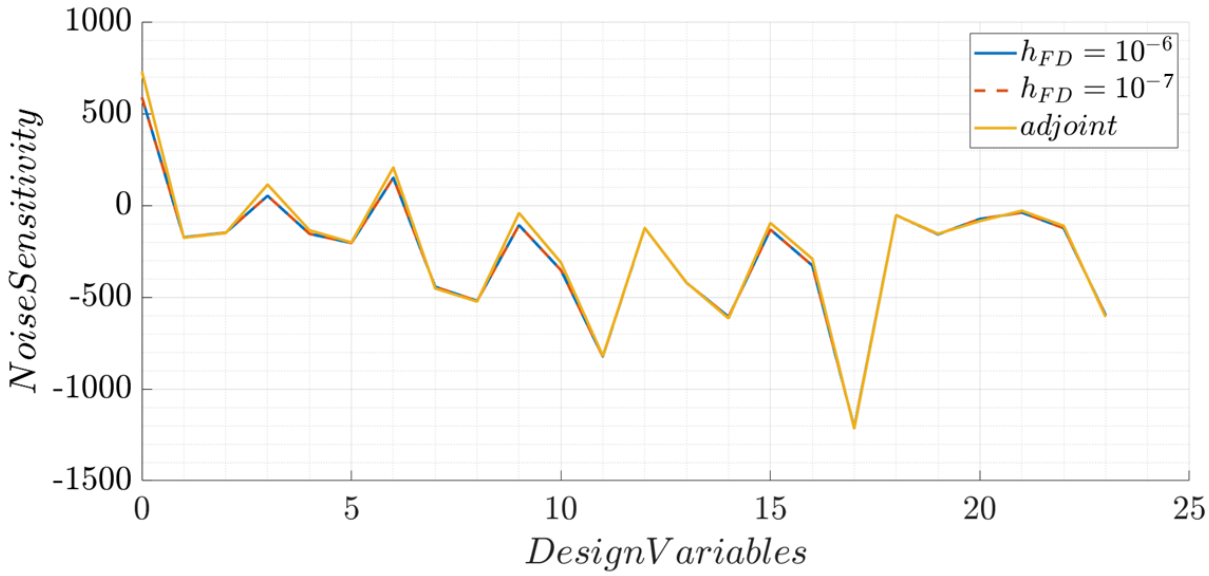

Figure 11: Noise Sensitivity for each Design Variable

5. Results

5.1. Noise Minimization

In this section the baseline two-bladed propeller presented in section 3 is optimized to reduce the emitted noise while keeping the thrust constant. The propeller is investigated in a forward flight condition, it rotates around the x-axis at $\omega = -523.598$ rad/s and the free-stream has a velocity of $U = 34.3m/s$. The computational mesh used in this section is the *Medium* grid used during the mesh convergence analysis in section 3. It uses periodic boundary conditions to account for the effect of the other propeller blade in the CFD simulation. The impermeable Di Francescantonio formulation is used to compute the noise signature of the blade. Moreover, the propeller reconstruction technique presented in section 2.3 is used to account for the noise of the other blade.
The objective function J shown in equation (21) is the sound pressure level (SPL). Only one observer is used to analyze the pressure fluctuation, it is located at a distance $d = 10R$, with R being the radius of the propeller at an incidence angle of 45°.

$$p_{rms,_{avg}} = \frac{1}{N_{obs}} \sum_{i=1}^{N_{obs}} p_{rms,_i} \tag{20}$$

$$J = 20\, log_{10} \left(\frac{p_{rms,_{avg}}}{p_0} \right), \quad p_0 = 20\, \mu Pa \tag{21}$$

The geometry is parametrized using one FFD box with 56 design variables that can move only along the freestream flow direction (x-axis). The mesh is deformed using a radial basis function (RBF) technique with 10% of the surface nodes as control points and Wendland C2 functions as the basis function following the work of Guardone et al [3]. By using this mesh deformation technique the connectivity is maintained.
The optimization is carried out for 18 design updates. Figure 12 shows the difference between the baseline and the optimized designs. In order to observe correctly the propeller deformation, the change of the blade section is reported for six stations at 35%, 50%, 65%, 80%, 90%, and 98% of the radius in Figure 14, their span-wise position is indicated in red in Figure 13. It can be observed that in every case the optimizer reduces the incidence angle of the section while increasing the camber. The thickness of the sections is not changed significantly even though no thickness constraints were imposed.

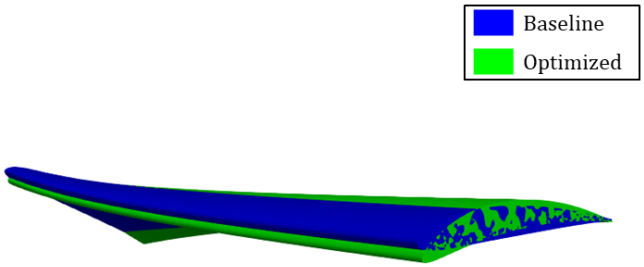

Figure 12: Blade Deformation

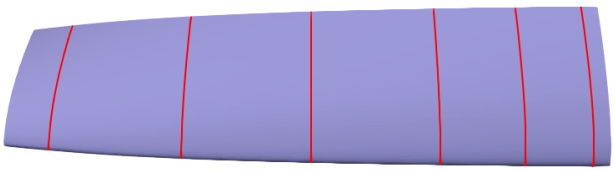

Figure 13: Monitored Sections Positions

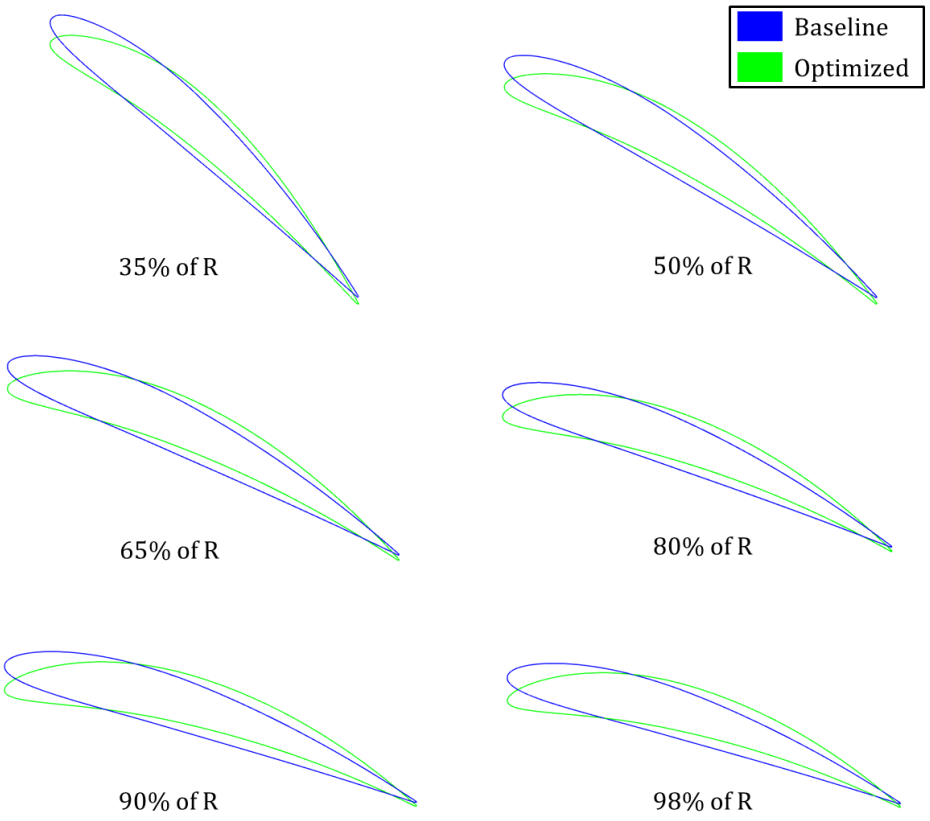

Figure 14: Propeller Sections Change

The results of the optimization are summarized in Table 3. The optimization achieves a 55% reduction in the objective function because the p_{rms} is reduced by 96%. Moreover, the C_{F_x} and C_{M_x} modulus are reduced by 3% and 72% respectively. During the problem definition the thrust coefficient (C_{F_x}) was constrained to remain constant but it can be observed that it has decreased, this happens because the constraint is enforced in a weak manner by using a penalty function method [14].

Table 3: Optimization Results

Parameter	**Baseline**	**Optimized**	**Change %**
SPL [dB]	52.42	23.18	-55.67
p_{rms}	8.352×10^{-3}	2.883×10^{-4}	-96.55
C_{F_x}	2.573×10^{-2}	2.494×10^{-2}	-3.07
C_{M_x}	2.354×10^{-3}	6.553×10^{-4}	-72.16

Figure 15 shows the comparison of the C_P curves between the baseline and the optimized designs at the 65% and 98% span sections. It can be observed that the space between the upper and the lower curves does not vary significantly, which explains why the thrust coefficient (C_{F_x}) stays almost constant, but the values of the C_P change, specially on the rear of the airfoil which may be the cause of the moment coefficient (C_{M_x}) decrease.

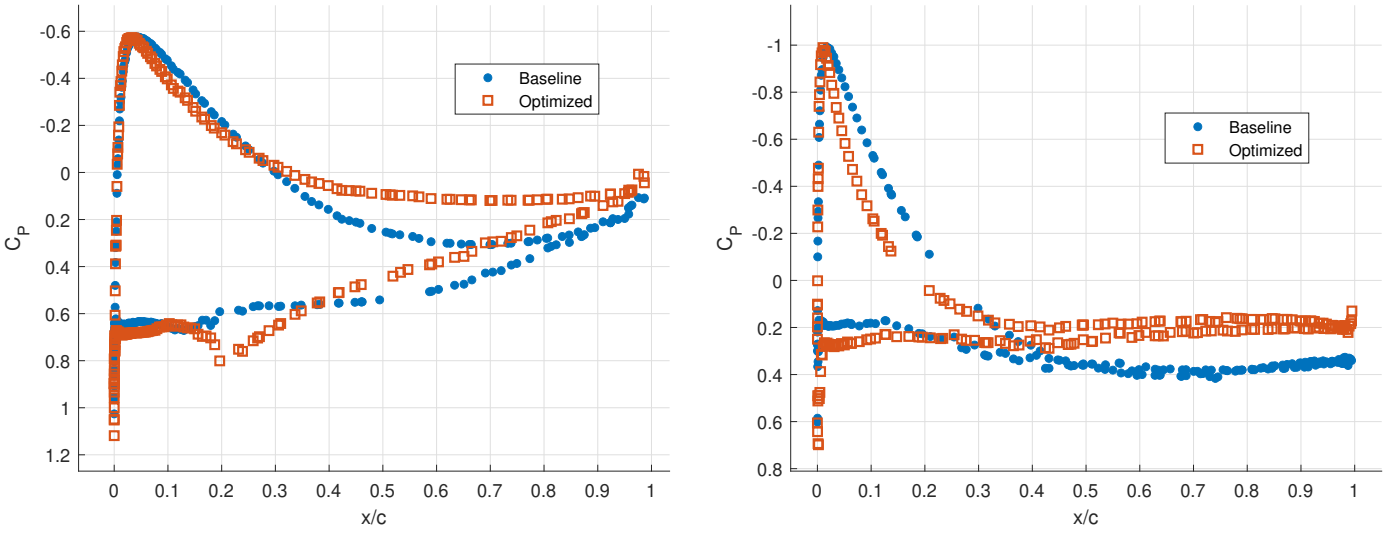

(a) 65 % Span (b) 98 % Span

Figure 15: C_P at different span locations

The pressure fluctuation and the FFT of the baseline and the optimized cases are analyzed at the observer location and shown in Figure 16. It can be observed that there is a dramatic change in amplitude for the pressure fluctuation signal, this is the reason why the p_{rms} has decreased so much. It can be noted in the FFT that the amplitude has been reduced at every frequency but the biggest change has been at the lower frequencies, which had the biggest amplitude. Moreover, the low frequency of the signal characteristics have been altered.

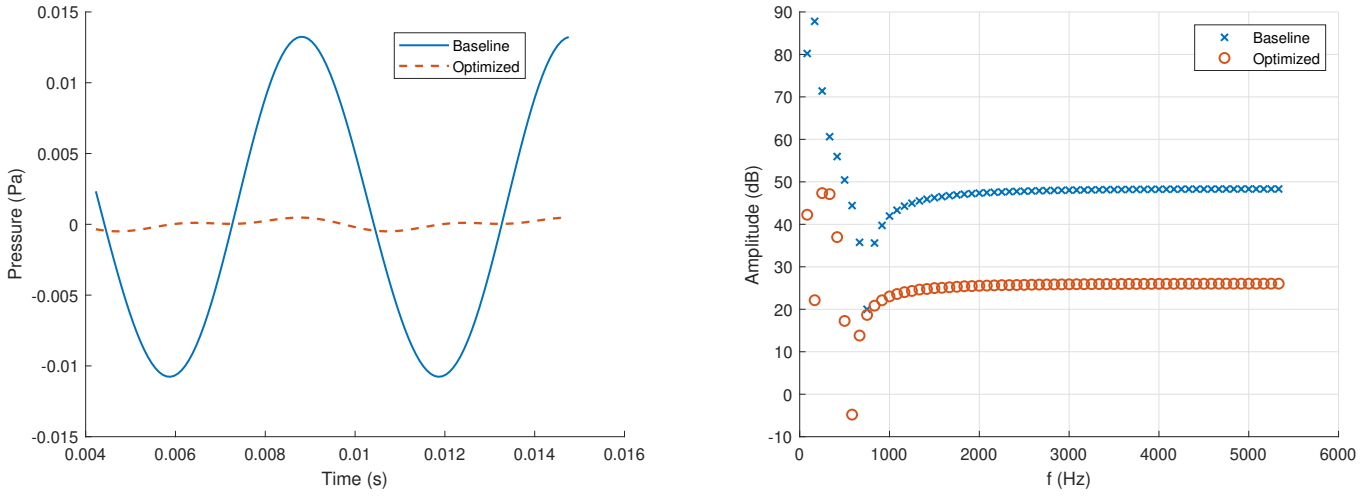

(a) Pressure Fluctuation (b) FFT

Figure 16: Acoustic Signature at 45° Observer

Figure 17 shows the SPL for both the baseline case and the optimized one at for two arrays of 10 microphones each placed at a distance of $d_1 = 10R$ and $d_2 = 30R$, with R being the radius of the propeller at an incidence angle from 45° to 135°. It can be observed that the SPL has been decreased at every observer location but since the microphone used for the optimization was placed at 45°, this is the position where the noise signature has been reduced the most. Moreover, it can be noted that as the distance increased the SPL is attenuated. At a distance $d_1 = 10R$ the average SPL was reduced by an 18.6% (10.9 dB) whereas at a distance $d_2 = 30R$ the average SPL was reduced by a 21.6% (10.5 dB). Therefore, the optimization works properly but it must be noted that the microphone position affects greatly the noise distribution of the optimized blade.

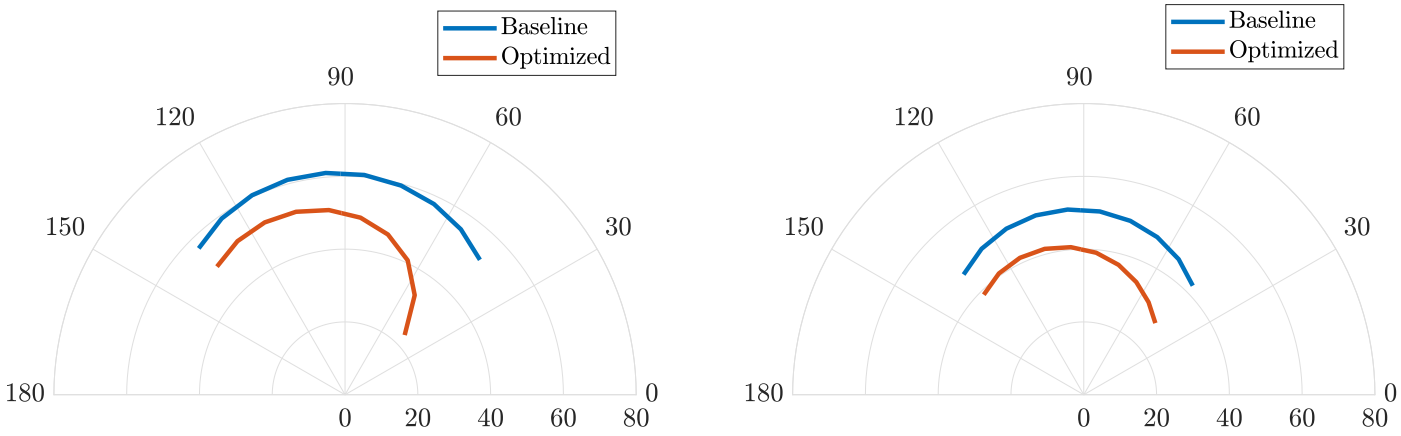

(a) SPL [dB] at 10R (b) SPL [dB] at 30R

Figure 17: Propeller Acoustic Signature Comparison $45° - 135°$ Observers

6. Conclusions

This work presented the progress carried out in the coupled CAA-CFD optimization framework inside the open-source multi-physics solver SU2 for cases with axial symmetry like propellers. In this framework the RANS equations are used to solve the flow around the body and the FW-H formulation propagates the pressure fluctuations to the farfield, then an AD-based discrete adjoint computes the sensitivities. The body was parametrized using a Free Form Deformation box, chosen for its capability to handle arbitrary shapes. The RANS equations are solved in a rotating reference frame (RRF), replacing the unsteady simulation by a steady simulation and a set of rigid rotations, lowering the computational cost. The successful application of periodic boundary conditions along the half-planes of radial symmetry in the CFD simulation opens the possibility of studying multi-blade propellers by just analyzing a single blade. Since the full propeller is needed for the acoustic simulation, a propeller reconstruction technique was implemented to account for the missing blades with successful results. The verification of the use of periodic boundary conditions in aeroacoustic analyses was carried out along with the validation of the aeroacoustic sensitivities using the AD-based discrete adjoint framework. An optimization case was conducted in which the shape of a propeller blade was modified to reduce the noise signature at a single observer location while keeping the thrust constant. The proposed framework reduced the average SPL by an 18.6% (10.9 dB) for a microphone array positioned at a distance of ten times the radius at an incidence angle from $45°$ to $135°$. It has also been noted that the position of the observer location used in the optimization affects significantly the noise directivity of the design.
In future work, concerning the CFD module, the results and the sensitivities obtained with the RANS simulations could be compared to the ones obtained using scale-resolving simulations such as DES to assess whether the lower fidelity alternatives reach an optimal configuration. Regarding the CAA module, the impermeable FW-H formulation could be replaced by the permeable FW-H formulation to be able to successfully study transonic cases.

References

[1] *Guide: Guide for the Verification and Validation of Computational Fluid Dynamics Simulations (AIAA G-077-1998(2002)).*

[2] Automatic differentiation of advanced cfd codes for multidisciplinary design. *Computing Systems in Engineering*, 3(6):625–637, 1992.

[3] Luca Abergo, Myles Morelli, and Alberto Guardone. *Aerodynamic Optimization based on a Discrete Adjoint Framework and Radial Basis Function Mesh Deformation in SU2.*

[4] Tim A. Albring, Max Sagebaum, and Nicolas R. Gauger. Efficient aerodynamic design using the discrete adjoint method in su2. *17th AIAA/ISSMO Multidisciplinary Analysis and Optimization Conference*, 2016.

[5] Lukas Asmer, Henry Pak, Prajwal Shivaprakasha, Bianca Schuchardt, Peter Weiand, Frank Meller, Christoph Torens, Dennis Becker, Chen Zhu, Karolin Schweiger, Andreas Volkert, and Roman Jaksche. Urban air mobility use cases, missions and technology scenarios for the horizonuam project. 08 2021.

[6] Kenneth S. Brentner and F. Farassat. Modeling aerodynamically generated sound of helicopter rotors. *Progress in Aerospace Sciences*, 39(2):83–120, 2003.

[7] I. Celik, U. Ghia, P. Roache, and C. Freitas. Procedure for Estimation and Reporting of Uncertainty Due to Discretization in CFD Applications. *Journal of Fluids Engineering*, 130(7), 07 2008.

[8] P. di Francescantonio. A new boundary integral formulation for the prediction of sound radiation. *Journal of Sound and Vibration*, 202(4):491–509, 1997.

[9] Thomas D. Economon, Francisco Palacios, and Juan J. Alonso. *A Viscous Continuous Adjoint Approach for the Design of Rotating Engineering Applications.*

[10] Thomas D. Economon, Francisco Palacios, and Juan J. Alonso. *A Viscous Continuous Adjoint Approach for the Design of Rotating Engineering Applications.* 2013.

[11] Thomas D. Economon, Francisco Palacios, Sean R. Copeland, Trent W. Lukaczyk, and Juan J. Alonso. Su2: An open-source suite for multiphysics simulation and design. *AIAA Journal*, 54(3):828–846, 2016.

[12] F. Farassat and M.K. Myers. Extension of kirchhoff's formula to radiation from moving surfaces. *Journal of Sound and Vibration*, 123(3):451–460, 1988.

[13] J. E. Ffowcs Williams, D. L. Hawkings, and Michael James Lighthill. Sound generation by turbulence and surfaces in arbitrary motion. *Philosophical Transactions of the Royal Society of London. Series A, Mathematical and Physical Sciences*, 264(1151):321–342, 1969.

[14] Barry W. Kort and Dimitri P. Bertsekas. A new penalty function method for constrained minimization. In *Proceedings of the 1972 IEEE Conference on Decision and Control and 11th Symposium on Adaptive Processes*, pages 162–166, 1972.

[15] Michael James Lighthill and Maxwell Herman Alexander Newman. On sound generated aerodynamically i. general theory. *Proceedings of the Royal Society of London. Series A. Mathematical and Physical Sciences*, 211(1107):564–587, 1952.

[16] Myles Morelli Luca Abergo, A. G. B. Y. *Aerodynamic optimization based on a discrete adjoint framework and radial basis function mesh deformation in SU2.*

[17] Myles Morelli Luca Galimberti, A. G. B. Y. *An efficient noise prediction implementation towards propeller design with SU2.*

[18] Siva Nadarajah and Antony Jameson. A comparison of the continuous and discrete adjoint approach to automatic aerodynamic optimization. In *38th Aerospace sciences meeting and exhibit*, page 667, 2000.

[19] William L. Oberkampf and Timothy G. Trucano. Verification and validation in computational fluid dynamics. *Progress in Aerospace Sciences*, 38(3):209–272, 2002.

[20] P. J. Roache. Perspective: A Method for Uniform Reporting of Grid Refinement Studies. *Journal of Fluids Engineering*, 116(3):405–413, 09 1994.

[21] Max Sagebaum, Tim Albring, and Nicolas R. Gauger. High-performance derivative computations using codipack, 2017.

[22] Beckett Zhou, Tim A. Albring, Nicolas R. Gauger, Carlos Ilario, Thomas D. Economon, and Juan J. Alonso. *Reduction of Airframe Noise Components Using a Discrete Adjoint Approach.*

Abstract in lingua italiana

Questo lavoro presenta il progresso compiuto nel framework di ottimizzazione CAA-CFD accoppiato dal risolutore multifisico open source SU2 per casi con simmetria assiale come le pale eliche. In questo framework le equazioni RANS vengono utilizzate per risolvere il flusso attorno al corpo, la formulazione FW-H propaga le fluttuazioni di pressione al campo lontano, quindi un adjoint discreto basato su AD calcola le sensibilità. Le equazioni RANS vengono risolte utilizzando un sistema di riferimento rotante (RRF), sostituendo la simulazione instabile con una simulazione stabile e un insieme di rotazioni rigide, riducendo il costo computazionale. L'applicazione riuscita delle condizioni al contorno periodiche lungo semipiani di simmetria radiale nella simulazione CFD apre la possibilità di studiare eliche multipala analizzando solo una singola pala. Queste tecniche vengono applicate a un caso di ottimizzazione in cui la forma di una pala dell'elica viene modificata per ridurre la firma del rumore in una singola posizione dell'osservatore mantenendo costante la spinta. Il framework proposto riduce fortemente il livello medio di pressione sonora (SPL) per un microfono posizionato a una distanza di dieci volte il raggi

Parole chiave: aeroacoustica, ottimizzazione, adjoint discreto, rumore di eliche

Acknowledgements

I would like to thank my Master's Thesis director Prof. Alberto Guardone for giving me the opportunity to face a real-world engineering project in a leading aerospace research group. I would also like to thank Ing. Luca Abergo for his help and counseling, he has helped me develop valuable skills that have improved my academic and professional background. This project has broaden my interests concerning the different disciplines of the aerospace field. Finally, I would also like to thank my friends and family for their support during this amazing experience. Even though the first year was difficult with the online classes, it has been an extremely valuable experience.